SCIENCE CHINA
Technological Sciences

•Article•

https://doi.org/10.1007/s11431-023-2553-5

Performance analysis and multi-objective optimization based on a modified irreversible Stirling cycle

XU Lei, YU MinJie, LIU ZhiChun & LIU Wei*

School of Energy and Power Engineering, Huazhong University of Science and Technology, Wuhan 430074, China

Received July 25, 2023; accepted November 15, 2023; published online May 28, 2024

The efficiency of the actual Stirling engine is much lower than the ideal Carnot cycle efficiency. To obtain more precise efficiency for Stirling engines, this paper proposes a modified Stirling cycle with a more accurate heat transfer process in Stirling engines based on a thermodynamic function called available potential. The finite-time thermodynamic method is used to analyze the model performance under constant heat source temperature, finite temperature difference heat transfer, and incomplete regenerative processes. A new polytropic process is introduced to model the heat transfer between the working fluid and external heat sources in which only heat above ambient temperature is converted into technical work. The regenerator is divided into numerous smaller heat reservoirs with individual temperature to analyze the incomplete regenerative processes. The expressions of the output power and thermal efficiency are obtained based on the modified irreversible Stirling cycle, and the effects of irreversible losses are analyzed to evaluate the performance of the proposed model. Results indicate that the efficiency of the modified cycle is much lower than that of the ideal Stirling cycle with an isothermal process. With the increase of the average heat transfer temperature difference, there exists an optimum value for the power of the irreversible cycle. The optimum power of the model was obtained for varying thermodynamic parameters by optimizing the average heat transfer temperature difference between the hot and cold sides. To optimize the irreversible model, the multi-objective optimization analysis is carried out based on NSGA-II, which results in an optimized output power of 40.87 kW and an optimized thermal efficiency of 44%.

stirling cycle, regenerative processes, isopotential processes, multi-objective optimization, finite time thermodynamics

Citation: Xu L, Yu M J, Liu Z C, et al. Performance analysis and multi-objective optimization based on a modified irreversible Stirling cycle. Sci China Tech Sci, 2024, 67, https://doi.org/10.1007/s11431-023-2553-5

1 Introduction

With the continuous advancement of science, technology, and ecological civilization, the global energy consumption has been on a steady rise [1,2]. However, the dependence on traditional fossil fuels has resulted in significant ecological damage and global warming [3]. Consequently, the promotion of renewable energy utilization and enhancement of energy efficiency [4,5] have emerged as pivotal strategies for sustainable energy development. Among a variety of energy utilization devices, the Stirling engine is particularly noteworthy due to its potential to convert heat into mechanical work with high theoretical efficiency. It offers numerous advantages such as low emissions, high energy efficiency, fuel flexibility, high specific work output, low noise levels, high reliability, and low maintenance requirements. The Stirling engine is ideally suited for small to medium power applications that involve renewable energy utilization [6], micro-cogeneration applications [7,8], space power system [9,10], and low-grade heat recovery [11]. This presents a promising field that warrants further exploration and research.

The Stirling engine, an external combustion engine invented by Robert Stirling in 1816 [12], operates based on a Stirling cycle, which consists of two isothermal and two isochoric processes. In an ideal scenario, the Stirling engine

*Corresponding author (email: w_liu@hust.edu.cn)

can convert heat into mechanical work with the Carnot efficiency, which is the maximum possible efficiency for any heat engine. However, in reality, there are many irreversible factors that prevent the Stirling engine from achieving this ideal efficiency. Therefore, the thermodynamic study of the irreversibility of the Stirling engine has never stopped. The finite-time thermodynamic (FTT) is a widely used thermodynamics analysis method for analyzing the irreversibility of heat engines in recent years.

Curzon and Ahlborn [13] were the first to apply FTTs to analyze heat engine in 1975. This approach differs from classical thermodynamic models as it takes into account the finite-time and finite-rate heat transfer, which can produce positive power output. Many researchers have since studied the FTT performance of Stirling engines, building upon the work of Curzon and Ahlborn. Assuming an ideal regenerator, they developed FTT models of Stirling engines by considering the thermal resistance between the working fluid and the external heat sources [14–20]. Blank et al. [14,16] analyzed an endo-reversible Stirling cycle with perfect regeneration using FTT and derived expressions for optimum power and efficiency at optimum power, based on the temperature bounds of the heat source and sink. Ladas and Ibrahim [15] utilized the FTT analysis to study how heat-transfer contact time and regeneration affect the Stirling cycle, conducting their analyses based on mass and energy balances associated with heat-transfer-rate equations. Senft [17] developed a mathematical model of an ideal Stirling engine with finite heat transfer and considered how internal thermal losses and mechanical losses affect its operation. The FTT approach provides a practical solution for analyzing the performance of Stirling heat engines.

The aforementioned models only take into account the finite rate of heat transfer between the Stirling heat engine and the external heat source. However, in practical scenarios, regenerative losses cannot be overlooked when simulating the actual operation of a Stirling engine, given that the regenerator is not perfect. As a result, a series of FTT models of Stirling engines that consider regenerative losses have been proposed to predict the performance of Stirling engines with greater accuracy. These models have been applied to various types of Stirling engines and have demonstrated improved accuracy and reliability [21–35]. Chen et al. [21,22] developed a more realistic model of the Stirling cycle that accounts for regenerative losses and explored their impact on the optimal performance of the engine. Wu et al. [23] determined the relationship between the power output and thermal efficiency by applying FTT to consider the irreversibility of heat transfer and imperfect regeneration. Kaushik and Kumar [24,25] also employed FTT to model the engine with finite heat capacity of the external reservoirs and examined how the effectiveness of various heat exchangers and regenerators influences its performance. Similarly, Tyagi et al. [26–28] modeled the irreversible Stirling refrigerator and heat pump cycle with finite temperature difference and regenerative losses. Ahmadi et al. [32] investigated how design parameters affect the performance of the engine with various sources of irreversibility: finite-rate heat transfer, regenerative loss, conductive thermal bridging loss, and finite regenerative time. Dai et al. [33,34] conducted a detailed thermodynamic study of the regenerative heat process by dividing the regenerator into smaller units, resulting in a more realistic model of Stirling engines.

In the above Stirling engine models, the compression and expansion processes of the working fluid are assumed to be isothermal. However, in reality, it is difficult to achieve an isothermal process due to the temperature difference between the working fluid and external heat sources. Therefore, the temperature of the working fluid in the expansion chamber and compression chamber of the Stirling engine will vary continuously [36–42]. Erbay and Yavuz [36] analyzed the real Stirling heat engine for maximum power output conditions by introducing polytropic processes and derived the relationship between two polytropic exponents during expansive and compressive processes. They [37,40] also studied the performance of duplex Stirling refrigerators with different constructions based on polytropic processes. Babaelahi and Sayyaadi [38] proposed a method to calculate polytropic exponents and improved differential control equations of the adiabatic model of Stirling engines to obtain a new polytropic model. Dai et al. [41,42] developed a polytropic model for the irreversible Stirling cycle and obtained corresponding polytropic exponents through thermodynamics analysis.

In addition to studying the irreversible losses of the Stirling engine to obtain a more accurate model, the selection of optimal operating parameters is also crucial for the design and performance improvement of the system. Numerous studies have been conducted to optimize the performance of Stirling engines. The common optimization methods include analytical methods that derive optimal solutions under optimal conditions and numerical methods that leverage intelligent computer operations [43]. He et al. [44] carried out an ecological optimization of the irreversible Stirling heat engine. Yaqi et al. [45] optimized an FTT model of a solar-powered Stirling engine for maximum power and obtained the corresponding efficiency at maximum power. However, there is often more than one objective to optimize in a thermodynamic system. Therefore, multi-objective optimization of various thermodynamic and energy systems using optimization algorithms has gained attention in recent years [46–56]. For example, Ahmadi et al. [46–49] performed multi-objective optimization of Stirling engine, Stirling refrigerator and Stirling heat pump using genetic algorithm with power, thermal efficiency and thermo-economic function as objective functions, respectively. Duan et al. [50]

applied particle swarm algorithm to optimize the irreversible model of Stirling engine to obtain a three-dimensional Pareto front and selected the optimal solution by linear programming technique for multidimensional analysis of preference (LINMAP). Toghyani et al. [51] used non-ideal adiabatic analysis and NSGA-II algorithm to optimize the efficiency and power loss for a Stirling system. Patel and Savsani [52] proposed TS-TLBO (tutorial training and self-learning inspired teaching-learning-based optimization) algorithm for the multi-objective optimization of a Stirling heat engine.

Due to the over-idealization of the isothermal processes, the efficiency of an actual Stirling heat engine is significantly lower than the theoretical Carnot efficiency. In this paper, we propose a new polytropic cycle for the Stirling engine, termed as the modified Stirling cycle, which simulates heat transfer between the working fluid and the external heat source with the isopotential processes. The modified Stirling cycle consists of two isochoric processes and two isopotential processes. The output power and thermal efficiency of the modified Stirling cycle are derived considering irreversible heat transfer both in the regenerative and isopotential processes under constant heat reservoirs with finite temperature difference. The effects of thermodynamic parameters such as regenerator effectiveness and average heat transfer temperature difference on the performance of the modified Stirling cycle are analyzed. The results indicate that there exists an optimal average heat transfer temperature difference between the hot and cold sides that maximizes the output power under a given operating condition. A multi-objective genetic algorithm is applied to optimize both power and efficiency simultaneously under different values of thermodynamic parameters.

2 System description

The Stirling engine operates ideally based on the Stirling cycle. The Stirling cycle consists of two isothermal processes and two isochoric regenerative processes. In an ideal isothermal process, all the heat absorbed from the external heat reservoirs is converted into technical work. However, for a real thermodynamic process, there are certain irreversible factors that affect the efficiency of the heat-work conversion. Moreover, the heat below the ambient temperature cannot be utilized in this process. Consequently, the actual performance of the Stirling engine deviates from the theoretical one. An availability function [57,58] is defined as a measure of the maximum useful work that can be produced by a system interacting with the environment, which can also be called available potential [59]:

$$e = h - T_0 s, \tag{1}$$

where h is enthalpy, s is entropy, and T_0 is ambient temperature. According to eq. (1), the available potential is calculated by deducting the unavailable thermal potential $T_0 s$ from the total potential h, which means only heat potential above ambient temperature could be used in a process.

Analogous to the isothermal, isobaric, isochoric, and isentropic processes in thermodynamics, a new thermodynamic process, called the isopotential process, can be described as

$$\mathrm{d}e = \mathrm{d}h - T_0 \mathrm{d}s = 0. \tag{2}$$

According to the definition in eq. (1), the isopotential process can represent a thermodynamic process, in which only the available energy converts into the technical work. For the ideal gas, eq. (2) becomes

$$c_p \mathrm{d}T - T_0 \mathrm{d}s = 0, \tag{3}$$

$$\frac{\mathrm{d}T}{\mathrm{d}s} = \frac{T_0}{c_p}, \tag{4}$$

where c_p is the constant pressure-specific heat capacity of the working fluid.

As depicted in eq. (4), there exists a linear correlation between temperature and entropy during the isopotential process. The gradient of the *T*-*s* curve is influenced by both the ambient temperature and the specific heat capacity of the working fluid. Consequently, the isopotential process can be likened to a polytropic process. Utilizing the isopotential process as a foundation, a novel polytropic model of the Stirling cycle can be established, incorporating two isopotential processes and two isochoric processes. This model is referred to as the modified Stirling cycle, as illustrated in Figure 1.

As illustrated in Figure 1, the temperature of the working fluid undergoes a continuous variation during the expansion and compression processes in the modified Stirling cycle. The formulation of the modified Stirling cycle is primarily contingent upon the designation of state points 1 and 3. Adhering to the principle that any two independent thermodynamic state parameters can ascertain a thermodynamic state, the thermodynamic states (T_1, v_1) and (T_3, v_3) of points 1 and 3 are initially determined by setting the temperature and specific volume. In accordance with the thermodynamic characteristics of the isopotential and isochoric processes, the specific volume and temperature of state points 2 and 4 can be respectively derived, as delineated in eqs. (5)–(8).

$$v_2 = v_1, \tag{5}$$

$$v_4 = v_3, \tag{6}$$

$$c_p(T_3 - T_2) = T_0\left[c_v \ln\left(\frac{T_3}{T_2}\right) + R_g \ln\left(\frac{v_3}{v_2}\right)\right], \tag{7}$$

$$c_p(T_1 - T_4) = T_0\left[c_v \ln\left(\frac{T_1}{T_4}\right) + R_g \ln\left(\frac{v_1}{v_4}\right)\right], \tag{8}$$

where c_v and R_g represent the constant specific heat capacity

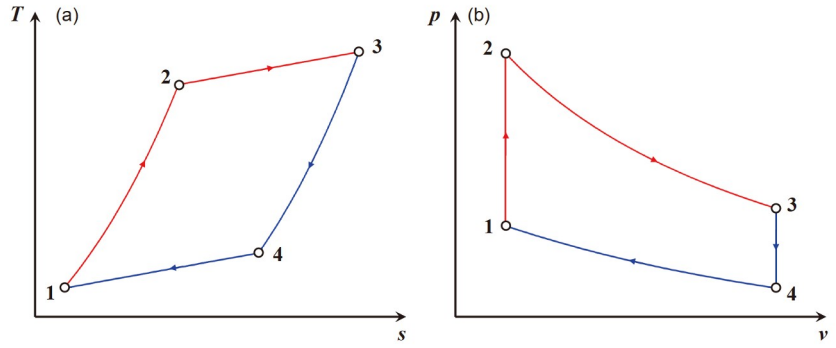

Figure 1 (Color online) Schematic diagram of the modified Stirling cycle. (a) Temperature-entropy diagram; (b) pressure-volume diagram.

and gas constant of the working fluid, respectively. From the above equations, the thermodynamic states of points 2 and 4 can be ascertained given that the thermodynamic states of points 1 and 3 are provided. Consequently, the thermodynamic states of each point within the cycle can be determined.

For the modified Stirling cycle, the heat absorbed and heat released in the isochoric processes 1–2 and 3–4 can be given respectively by

$$q_{1-2} = c_v(T_2 - T_1), \tag{9}$$

$$q_{3-4} = c_v(T_3 - T_4). \tag{10}$$

On the *T*-*s* diagram of the cycle, it can be discerned that the average slope of the *T*-*s* curve in process 1–2 is less steep than that of the curve in process 3–4, which implies that the temperature difference between state points 1 and 2 is more pronounced than that of state points 3 and 4. This confirms that the heat absorbed during the isochoric process 1–2 exceeds the heat released during the isochoric process 3–4. Therefore, in contrast to the ideal Stirling cycle, the regeneration is not perfect in the reversible modified Stirling cycle. According to the definition of entropy, the heat absorbed from the heat source and heat released to the heat sink in the isopotential processes 2–3 and 4–1 can be respectively articulated as

$$q_{2-3} = \int_{s_2}^{s_3} T\mathrm{d}s = \int_{T_2}^{T_3} c_p \frac{T}{T_0}\mathrm{d}T = \frac{c_p}{2T_0}\left(T_3^2 - T_2^2\right), \tag{11}$$

$$q_{4-1} = -\int_{s_4}^{s_1} T\mathrm{d}s = \int_{T_1}^{T_4} c_p \frac{T}{T_0}\mathrm{d}T = \frac{c_p}{2T_0}\left(T_4^2 - T_1^2\right). \tag{12}$$

Coupling eqs. (9)–(12), the thermal efficiency of the modified Stirling cycle with imperfect regeneration can be expressed as

$$\eta^{th} = 1 - \frac{q_{41}}{q_{12} + q_{23} - q_{34}} = 1 - \frac{c_p\left(T_4^2 - T_1^2\right)}{c_p\left(T_3^2 - T_2^2\right) + 2c_v\left[(T_2 - T_1) - (T_3 - T_4)\right]T_0}. \tag{13}$$

3 Thermodynamic analysis with FTT

A reversible cycle is composed of several reversible processes, and these processes must be quasi-static, implying that the cycle takes an infinite duration and yields no power output. However, in a real thermodynamic cycle, all processes are irreversible and possess finite durations and heat transfer rates. In this section, we consider the finite-rate heat transfer between the working fluid and the external heat reservoirs and regenerator. Based on FTTs, a theoretical model of the irreversible modified Stirling cycle is developed.

Figure 2 shows the *T*-*s* schematic of the irreversible modified Stirling cycle model. The heat source and heat sink maintain constant temperatures T_H and T_L, respectively, and the working fluid is an ideal gas. Over a finite duration, due to thermal resistance, the working fluid exhibits different temperatures from the heat source and sink.

The cycle consists of four processes. Process 1–2 is an isochoric process where the working fluid absorbs heat from the regenerator. Process 2–3 is an isopotential process where the working fluid absorbs heat from the heat source, causing its temperature to ascend from T_2 to T_3; Process 3–4 is an isochoric process where the working fluid discharges heat to the regenerator. Process 4–1 is an isopotential process where the working fluid releases heat to the heat sink, leading to a temperature decrease from T_4 to T_1. Due to imperfect regeneration, the outlet states of the working fluid in the regenerator are at 2′ instead of 2 and 4′ instead of 4, respectively.

According to heat transfer theory, the rate of heat absorbed from and released into the working substance are proportional to the temperature differences between the working substance and external heat reservoirs. It is assumed that the heat transfer rate is proportional to the arithmetic mean temperature difference between the working fluid and external heat reservoirs, denoted as

$$Q_H = \alpha_h \delta T_H t_h, \tag{14}$$

$$Q_L = \alpha_l \delta T_L t_l, \tag{15}$$

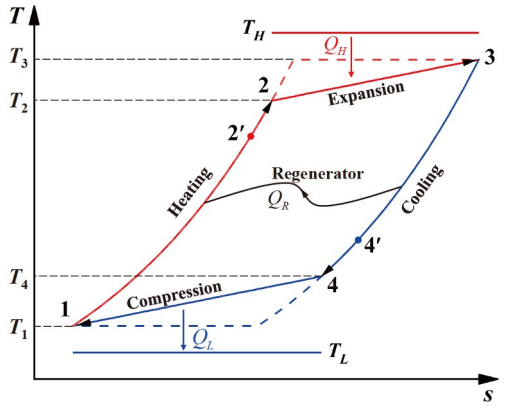

Figure 2 (Color online) The *T*-*s* diagram of the irreversible modified Stirling cycle.

where α_h and α_l denote the thermal convection performance between working fluid and heat source at temperature T_H and heat sink at temperature T_L, respectively. t_h and t_l represent the heat addition and heat rejection times for the irreversible modified Stirling cycle, respectively. The average heat transfer temperature difference δT_H, δT_L is defined as

$$\delta T_H = T_H - \frac{T_2+T_3}{2}, \tag{16}$$

$$\delta T_L = \frac{T_1+T_4}{2} - T_L. \tag{17}$$

Process 2–3 and process 4–1 are isopotential processes; thus the heat exchange between working fluid and heat reservoirs in the expansion and compression processes can be expressed respectively as

$$Q_h = \int_{T_2}^{T_3} mc_p \frac{T}{T_0} \mathrm{d}T = \frac{mc_p}{2T_0}\left(T_3^2 - T_2^2\right), \tag{18}$$

$$Q_l = -\int_{T_4}^{T_1} mc_p \frac{T}{T_0} \mathrm{d}T = \frac{mc_p}{2T_0}\left(T_4^2 - T_1^2\right), \tag{19}$$

where m, c_p, and T_0 denote mass of the working substance, constant pressure specific heat capacity, and ambient temperature, respectively.

In addition to the temperature difference between the working fluid and the external heat reservoirs, a temperature difference also exists between the working fluid and the regenerator. In practical applications, the Stirling engine operates at a high frequency, causing the working mass to flow through the regenerator rapidly. This results in an uneven temperature distribution within the regenerator. To analyze the heat transfer process with a finite temperature difference, we assume that the regenerator consists of numerous smaller heat reservoirs, each with a distinct temperature. During the regenerative processes, the working fluid sequentially contacts these heat reservoirs. Given that the working fluid has a significantly lower heat capacity than the regenerator in a Stirling engine, it is assumed that each sub-regenerator maintains a constant temperature as the working fluid passes through it.

Figure 3 presents a schematic diagram of the heat transfer between the working fluid and the sub-regenerators during the regenerative cooling process. It is assumed that the regenerator is composed of n sub-regenerators, with a temperature difference of ΔT_{rl} between each pair of adjacent sub-regenerators. Consequently, the temperature of the sub-regenerators varies from $T_3 - \Delta T_{rl}$ to $T_4 + \Delta T_{rl}$. Due to the finite heat transfer rate, the temperature drop of the working fluid after passing through each sub-regenerator is less than the temperature difference between each pair of adjacent sub-regenerators. As depicted in Figure 3, the temperature drop rate of the working fluid escalates with an increase in the temperature difference between the working fluid and the sub-regenerators. Defining the entire duration of the regenerative cooling process as t_{rl}, the duration of heat transfer between the working fluid and each sub-regenerator is Δt_{rl}. As a result, we can derive the following relationship:

$$\Delta T_{rl} = \frac{T_3 - T_4}{n+1}, \tag{20}$$

$$\Delta t_{rl} = \frac{t_{rl}}{n}. \tag{21}$$

The temperature of the i^{th} sub-regenerator $T_{r,i}$ can be expressed as

$$T_{r,i} = T_3 - i \cdot \Delta T_{rl} = T_3 - \frac{T_3 - T_4}{n+1} i, \quad i = 1, 2, ..., n. \tag{22}$$

The temperatures of the working fluid and the i^{th} sub-regenerator are denoted by T_f and $T_{r,i}$ respectively, According to Newton's law of cooling, the heat transfer between the working fluid and the i^{th} sub-regenerator is as follows:

$$\delta Q_i = \alpha_r \left(T_f - T_{r,i}\right) \mathrm{d}t, \quad i = 1, 2, ..., n, \tag{23}$$

where α_r denotes the thermal convection between working fluid and the regenerator.

In the regenerative cooling process, the heat absorbed from the working fluid is equal to the change in internal energy, with the following relationship:

$$\delta Q_i = -mc_v \mathrm{d}T_f = -C_v \mathrm{d}T_f, i = 1, 2, ..., n, \tag{24}$$

where $C_v = mc_v$ refers to the isochoric heat capacity of the working fluid.

Combining eqs. (23) and (24), the differential expression for t_{rl} can be obtained as

$$\mathrm{d}t = \frac{-C_v \mathrm{d}T_f}{\alpha_r (T_f - T_{r,i})}, i = 1, 2, ..., n. \tag{25}$$

The temperatures of the working fluid first flowing through the regenerator is T_3. It is assumed that the outlet temperature of the working fluid after cooling through the i^{th} sub-regenerator is $T_{f,i}$. Comparing the initial and final states of the working fluid in the i^{th} regenerative process, the

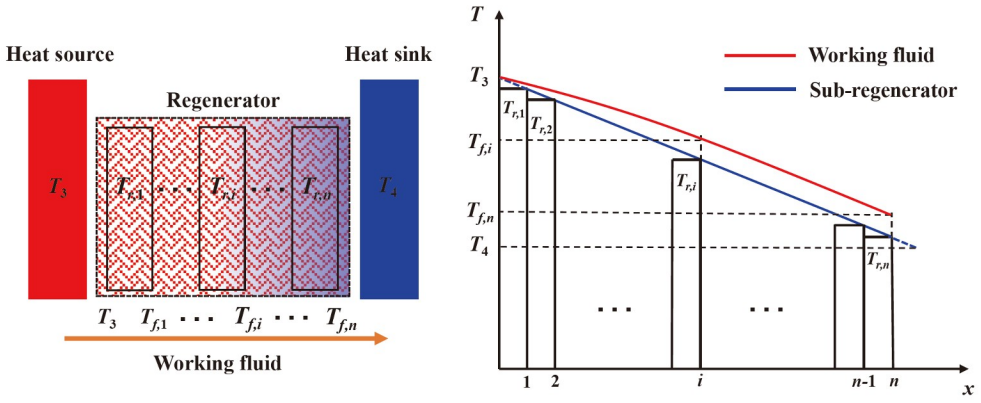

Figure 3 Schematic diagram of temperature difference in regenerative cooling process.

integration of eq. (25) gives

$$\frac{T_{f,i}-T_{r,i}}{T_{f,i-1}-T_{r,i}}=\exp\left(-\alpha_r t_{rl}/nC_v\right), i=1,2,...,n. \tag{26}$$

Substituting eq. (22) into eq. (26), the expression for the temperature of the working fluid after leaving the n^{th} sub-regenerator can be obtained by iteration as follows:

$$T_{f,n}=T_3+\frac{T_3-T_4}{n+1}\times\left[n+\left(1-\exp\left(-\alpha_r t_{rl}/C_v\right)\right)/\left(1-\exp\left(\alpha_r t_{rl}/nC_v\right)\right)\right]. \tag{27}$$

Then the efficiency of the regenerator in the regenerative cooling process is

$$\varepsilon_{rl}=\frac{T_3-T_{f,n}}{T_3-T_4}=\frac{n+\left[1-\exp\left(-\alpha_r t_{rl}/C_v\right)\right]/\left[1-\exp\left(\alpha_r t_{rl}/nC_v\right)\right]}{n+1}. \tag{28}$$

In reality, the temperature is not uniformly distributed throughout the entire regenerator. Therefore, we postulate that the regenerator is divided into an infinite number of sub-regenerators, i.e., $n\to\infty$, thus the regenerative cooling efficiency can be simplified as

$$\varepsilon_{rl}=1-\left(\alpha_r t_{rl}/C_v\right)\cdot\left[1-\exp\left(-\alpha_r t_{rl}/C_v\right)\right]. \tag{29}$$

Similarly, when the duration of the regenerative heating process is t_{rh}, the regenerative heating efficiency can be obtained as follows:

$$\varepsilon_{rh}=1-\left(\alpha_r t_{rh}/C_v\right)\cdot\left[1-\exp\left(-\alpha_r t_{rh}/C_v\right)\right]. \tag{30}$$

According to the regenerative efficiency of the heating and cooling processes, the heat absorbed and released by the working fluid in the regenerator can be described as

$$Q_{rh}=mc_v\varepsilon_{rh}(T_2-T_1), \tag{31}$$

$$Q_{rl}=mc_v\varepsilon_{rl}(T_3-T_4). \tag{32}$$

Owing to the thermal characteristics of the regenerator, the heat exchange between the working fluid and the regenerator during the heating process should be equivalent to that during the cooling process. By integrating eqs. (31) and (32), the correlation between the regenerative efficiency of the heating and cooling processes can be articulated as

$$\varepsilon_{rh}=\frac{T_3-T_4}{T_2-T_1}\varepsilon_{rl}. \tag{33}$$

Therefore, the actual amounts of heat absorbed from the heat source and released into the heat sink for the irreversible modified Stirling cycle with imperfect regeneration are

$$Q_H=Q_h+mc_v(1-\varepsilon_{rh})(T_2-T_1), \tag{34}$$

$$Q_L=Q_l+mc_v(1-\varepsilon_{rl})(T_3-T_4). \tag{35}$$

Combining eqs. (14)–(19), and (34), (35), the durations of heat exchange between the working fluid and the external heat reservoirs can be expressed respectively as

$$t_h=\frac{c_p m\left(T_3^2-T_2^2\right)+c_v mT_0(1-\varepsilon_{rh})(T_2-T_1)}{\alpha_h T_0(2T_H-T_2-T_3)}, \tag{36}$$

$$t_l=\frac{c_p m\left(T_4^2-T_1^2\right)+c_v mT_0(1-\varepsilon_{rl})(T_3-T_4)}{\alpha_l T_0(T_1+T_4-2T_L)}. \tag{37}$$

The cycle period is composed of the durations of heat exchange with the external heat reservoirs and the times of the two regenerative processes, which can be expressed as

$$\tau=t_h+t_l+t_{rh}+t_{rl}. \tag{38}$$

According to the above equations, the output power and thermal efficiency of the irreversible modified Stirling cycle can be obtained as

$$P=\frac{Q_H-Q_L}{\tau}=\frac{mc_p\left(T_3^2+T_1^2-T_2^2-T_4^2\right)+2mc_vT_0(T_2+T_4-T_1-T_3)}{2T_0(t_h+t_l+t_{rh}+t_{rl})}, \tag{39}$$

$$\eta=\frac{Q_H-Q_L}{Q_H}=\frac{c_p\left(T_3^2+T_1^2-T_2^2-T_4^2\right)+2c_vT_0(T_2+T_4-T_1-T_3)}{c_p\left(T_3^2-T_2^2\right)+2c_vT_0(1-\varepsilon_{rh})(T_2-T_1)}. \tag{40}$$

4 Results and discussion

4.1 The modified reversible Stirling cycle model

Herein, a case study is conducted to compare the thermodynamic performance of Stirling engines based on the reversible modified Stirling cycle and the ideal Stirling cycle under identical parameter conditions. Helium is selected as the working fluid and other parameters are set as [60]: T_3 =922 K, T_1=288 K, v_1=0.2 m^3/kg, v_3=0.35 m^3/kg, T_0=300 K. The corresponding *T*-*s* and *p*-*v* diagrams of the reversible modified Stirling cycle and the ideal Stirling cycle are plotted in Figure 4.

In Figure 4, the dashed and solid lines represent the ideal and reversible modified Stirling cycles, respectively. The latter exhibits a smaller enclosed area than the former. During the isopotential process, the work performed by the working fluid is equivalent to its available energy. Contrary to an isothermal process, an isopotential process does not utilize thermal energy below ambient temperature, as depicted by curves 2–2′, 2–3, and 3–2′ in Figure 4. According to Figure 4, the working fluid commences heat absorption from the heat source prior to attaining the maximum temperature. The temperature of the working fluid escalates during the heat absorption process and culminates at the maximum temperature at the conclusion of the isopotential process 2′–3. Upon reaching state point 4′, the working fluid initiates heat release to the heat sink, with its temperature persistently decreasing during process 4′–1.

The efficiencies of the modified Stirling cycle, Stirling cycle, and experimental data under identical operating conditions are 41.53%, 68.76%, and 24.80%. The experimental data were extracted from literature data [60] for the maximum thermal efficiency in the same temperature range. As inferred from these data, although the efficiency of the modified Stirling cycle proposed in this study is significantly lower than that of the ideal Stirling cycle, it surpasses that of the actual Stirling heat engine.

To delve deeper into the disparity in energy conversion performance, Figure 5(a) and (b) juxtapose the energy conversion and thermal efficiency of the reversible modified Stirling cycle and the ideal Stirling cycle under varying temperature conditions. In Figure 5(a), the maximum temperature oscillates between 900 and 1100 K, while in Figure 5(b), the minimum temperature ranges from 320 to 400 K. As depicted in Figure 5(a), both cycles exhibit enhanced thermal efficiency with an increase in the maximum temperature. Conversely, Figure 5(b) illustrates that both cycles demonstrate diminished thermal efficiency as the minimum temperature escalates. In both scenarios, the thermal efficiency of the modified Stirling cycle is significantly lower than that of the ideal Stirling cycle.

In comparison to the ideal Stirling cycle, the modified Stirling cycle exhibits augmented heat absorption and exhalation per unit mass of working fluid under identical parameter conditions. However, the surge in the quantity of heat released by the working fluid considerably outweighs the amount of heat absorbed. This indicates that the heat discharged by the working fluid to the cooler in an actual heat engine exceeds the theoretical value of the Stirling cycle, resulting in a substantial reduction in actual heat engine efficiency compared with Carnot efficiency. Consequently, the efficiency of the modified Stirling cycle is closer to the actual Stirling heat engine, which is lower than that of the ideal Stirling cycle with an isothermal process. This can serve as a valuable guide for designing and optimizing actual Stirling heat engines.

4.2 The modified irreversible Stirling cycle model

A thorough performance analysis of the irreversible modified Stirling cycle model is conducted based on the numerical calculation depicted in Figure 6. The process com-

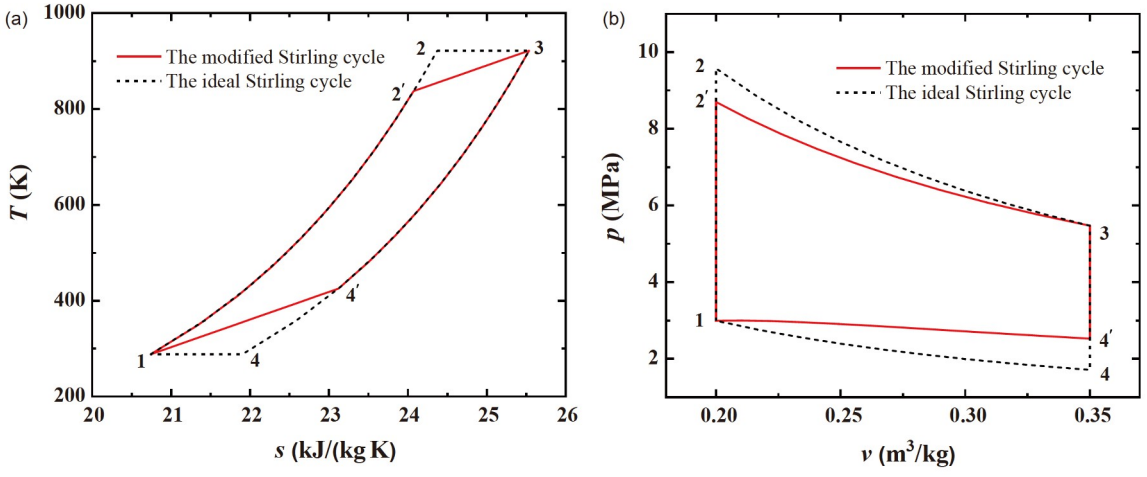

Figure 4 (Color online) (a) *T*-*s* and (b) *p*-*v* diagrams of the reversible modified Stirling cycle compared with the ideal Stirling cycle.

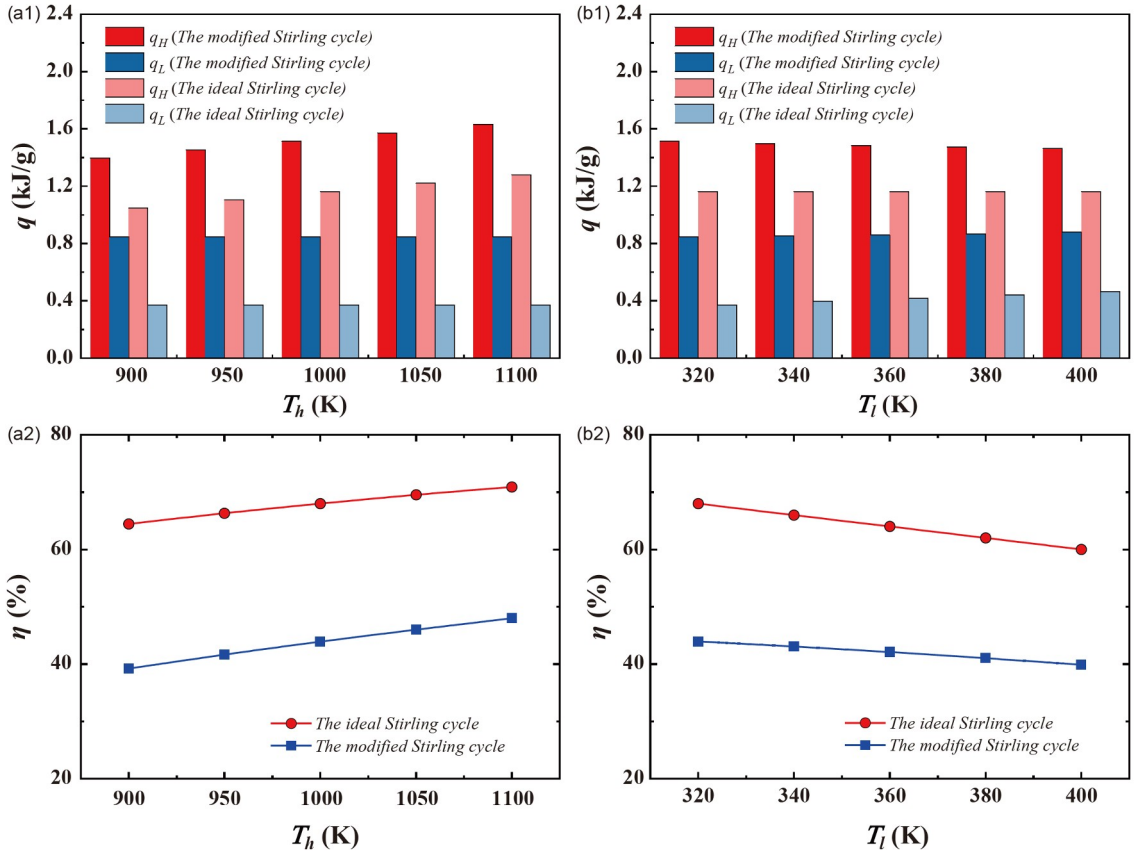

Figure 5 Comparison of energy conversion and thermal efficiency at different temperatures. (a) Maximum cycle temperature; (b) minimum cycle temperature.

mences with the initialization of the cycle's operating parameters and external parameters. Subsequently, the average heat transfer temperature differences, δT_H and δT_L, are input to compute the temperature at each state of the cycle. This is followed by two iterative processes employed to identify the operating temperatures of state points 1, 2, 3, and 4 of the modified Stirling cycle that correspond to the input temperature differences. In each iterative process, we initialize the temperatures of state points 3 and 1 respectively, and then solve eqs. (14) and (15) to obtain the temperatures of state points 2 and 4. Ultimately, we verify eqs. (7) and (8) using the obtained temperatures and update T_3 and T_1 accordingly until we achieve consistent values for T_1, T_2, T_3 and T_4 that satisfy the input δT_H and δT_L.

Upon determining the temperatures of each state point of the modified Stirling cycle, the efficiency of the regenerative process can be computed by incorporating the duration of the regenerative cooling process. Ultimately, the thermal performance of the modified Stirling cycle is assessed by resolving eqs. (39) and (40) for power and thermal efficiency.

4.2.1 Case analysis

The parameters in Table 1 are selected to analyze the performance of the modified irreversible Stirling cycle model.

The case analysis results, derived using the parameters outlined in Table 1 and the numerical calculation flow depicted in Figure 6, are presented in Table 2. The corresponding *T-s* and *p-v*, along with the energy consumption distribution, are further illustrated in Figure 7. As observed in Figure 7(a), the working fluid temperature escalates from 335.45 K at state point 1 to 855.96 K at state point 2, attributable to heat absorption from the regenerator matrix and heat sources. Subsequently, it further elevates to 944.04 K at state point 3 due to heating by the heat source during the isopotential expansion process. Following this, the temperature diminishes to 464.55 K at state point 4 as a result of the regenerative cooling process. Ultimately, it reverts to the initial state point 1 by discharging heat to the heat sink during the isopotential compression process.

Table 2 also reveals that the regenerative efficiency of the heating and cooling processes amounted to 88.52% and 96.10%, respectively. The discrepancy in regenerative efficiency between the heating and cooling processes stems from the characteristics of the isopotential process. As illustrated in Figure 7, the rate of energy input from the heat source was 87.03 kW. Discounting the heat loss attributable to imperfect regenerative heating, the net heat absorption of the working fluid from the heat source constituted 88.05% of

Table 1 Parameters of case analysis

Parameters	Values
Working substance	Helium
Mass of working substance m	2 g
Specific heat capacity c_p	5.2 kJ/(kg K)
Ideal gas constant R_g	2.077 kJ/(kg K)
Heat source temperature T_H	1000 K
Heat sink temperature T_L	300 K
Ambient temperature T_0	300 K
Average heat transfer temperature difference δT_H	100 K
Average heat transfer temperature difference δT_L	100 K
Coefficient of heat transfer α_h	2.0 kW/K
Coefficient of heat transfer α_l	2.0 kW/K
Coefficient of heat transfer α_r	20 kW/K
Duration of the regenerative cooling process t_{rl}	8×10^{-3} s
Volume compression ratio λ	1.8

the total heat absorption. Conversely, during the cooling stage of the working fluid, a mere 3.75% of the total heat absorption was lost due to imperfect regeneration, while 38.90% was converted into output power and 57.35% was transferred to the heat sink. The output power and thermal efficiency of the modified Stirling cycle were 33.86 kW and 38.90%, respectively.

4.2.2 *Parametric study*

Figure 8 illustrates the impact of the average heat transfer temperature difference on the hot side on the model performance under varying heat source temperatures. As depicted in Figure 8(b) and (c), with the heat transfer temperature difference on the hot side incrementally rising from 80 to 220 K, the power exhibits a non-linear trend, initially increasing and subsequently decreasing, while the thermal efficiency demonstrates a declining trend. At a heat source temperature of 1100 K, the power escalates from approximately 32 to 37 kW, thereafter diminishing to 36 kW, while the thermal efficiency decreases from 44% to 39%. As the temperature of the heat source escalates, both the power and thermal efficiency exhibit an upward trend. Figure 8(a) plots the cyclic *T-s* diagrams for cases with an average temperature difference on the hot side of 80, 120, and 160 K for heat source temperatures of 1000, 1050, and 1100 K, respectively.

In accordance with Newton's law of cooling, a higher temperature difference between heat transfer objects accelerates the rate of heat transfer. Thus, increasing the hot side average heat transfer temperature difference speeds up the heat transfer between the working fluid and the heater, thereby shortening the cycle period and enhancing the power. However, as indicated in Figure 8(a), with an increase in the average heat transfer temperature difference at the hot side from 80 to 160 K, the temperature level on the hot side diminishes, as does the area enclosed by the cycle. This results in a reduction in the output work of the cycle and a decrease in power output. Therefore, when δT_H is low, a shorter cycle time dominates, leading to an increase in power. Conversely, when δT_H is high, a smaller output work dominates and causes a decrease of power. As demonstrated in Figure 8(a), increasing δT_H also reduces the average temperature level at the hot side of the cycle, thus diminishing the temperature difference between the hot and cold sides of the cycle and decreasing the thermal efficiency. When δT_H is 120 K and the heat source temperature escalates from 1000 to 1100 K, the output power rises from 30.4 to 35.7 kW, and the thermal efficiency increases from 37.9% to 42.3%. This indicates that an increase in heat source temperature significantly enhances cycle performance.

Figure 9 delineates the influence of the average heat

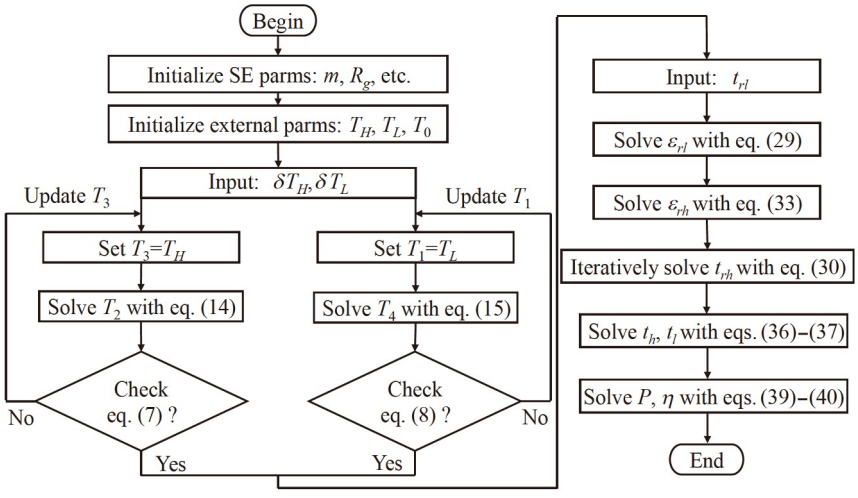

Figure 6 Flow chart of numerical calculation for the irreversible modified Stirling cycle.

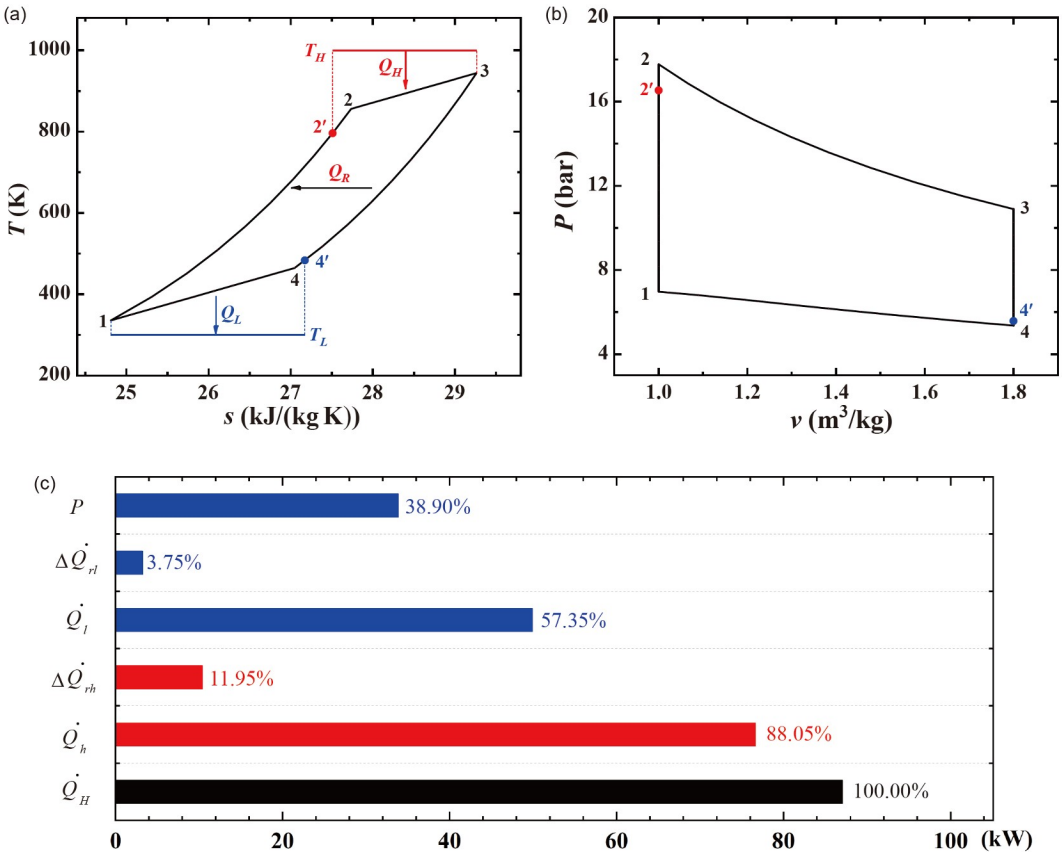

Figure 7 (Color online) (a) *T-s*, (b) *p-v* diagrams and (c) energy consumption distribution of case study.

Table 2 Results of case analysis

Circulation Temperature	T_1(K)	T_2(K)	T_3(K)	T_4(K)
	335.45	855.96	944.04	464.55
Model Performance	P(kW)	η(%)	ε_{rl}(%)	ε_{rh}(%)
	33.86	38.90	96.10	88.52

transfer temperature difference on the cold side on the cycle performance under varying heat sink temperatures. Figure 9 (b) and (c) show that an increase in the average heat transfer temperature difference on the cold side results in a peak in output power, while the thermal efficiency consistently declines. A higher heat sink temperature corresponds to lower power and thermal efficiency of the cycle.

Figure 9(a) plots the cyclic *T-s* diagrams under the average temperature difference at the cold side of 80, 120, and 160 K and the heat sink temperatures of 275, 300, and 325 K, respectively. As Figure 9(a) illustrates, a higher heat sink temperature elevates the cold side temperature and reduces the cycle work output, adversely affecting both power output and thermal efficiency. In Figure 9(a), a larger average heat transfer temperature difference at the cold side also increases the cold side temperature and decreases the cycle work output. Moreover, it shrinks the heat transfer temperature ranges of the working fluid at both sides under an identical heat sink temperature, leading to a decrease in cycle thermal efficiency. However, a higher cold side temperature enhances the heat transfer rate and reduces the cycle time. The power output is calculated by dividing work output by cycle time. The conflicting effects of these factors result in a peak in power output.

Figure 10 shows the effects of the regenerative cooling time on power and thermal efficiency of the cycle. As the regenerative time increases, the thermal efficiency continues to rise, albeit at a decelerating rate, while the power decreases with its rate of decline also slowing down. This phenomenon can be attributed to the fact that when the working fluid flows through the regenerator, a longer regenerative time implies more heat being exchanged between

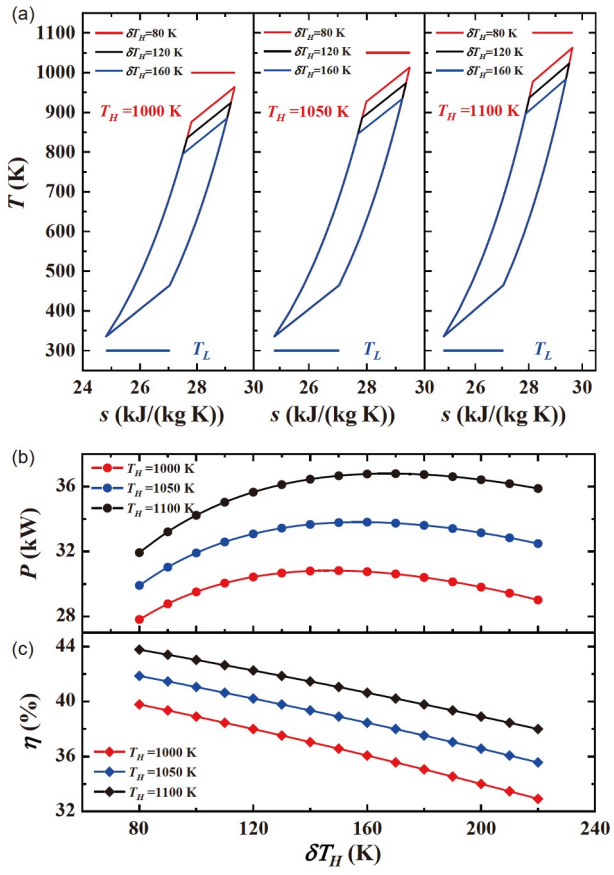

Figure 8 Model performance at varying hot-side arithmetic mean temperature difference and heat source temperatures. (a) Comparison of *T-s* diagrams; (b) power; (c) thermal efficiency.

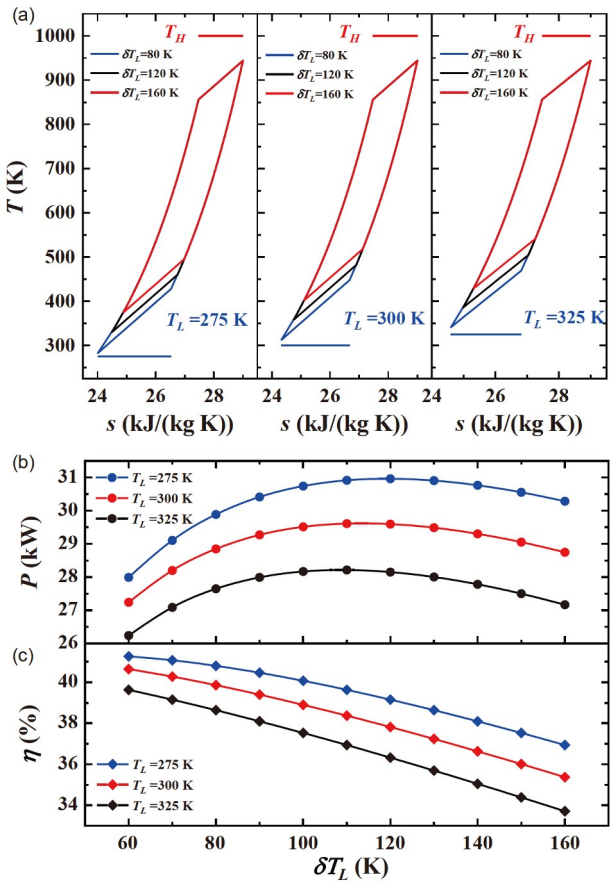

Figure 9 Model performance at different cold-side arithmetic mean temperature difference and heat sink temperatures. (a) Comparison of *T-s* diagrams; (b) power; (c) thermal efficiency.

the fluid and the regenerator, leading to a higher regenerative efficiency and consequently a higher thermal efficiency. However, beyond a certain point, the regenerative process approaches perfection and both values tend to stabilize. Although a longer regenerative time also augments the output work, it results in an extended cycle period, which in turn diminishes the power. Therefore, there exists a trade-off between power and thermal efficiency that hinges on the optimal selection of regenerative time.

As depicted in Figure 10(a) and (b), thermal efficiency decreases with increasing ambient temperature. This is due to the fact that an increase in ambient temperature results in an augmentation of unavailable thermal energy during the heat exchange process between the working fluid and the external heat reservoirs, which subsequently leads to a reduction in output work and cycle thermal efficiency. As observed in Figure 10(c) and (d), both power and thermal efficiency ascend with an increasing heat transfer coefficient between the working fluid and the regenerator. A superior heat transfer coefficient enhances the heat exchange between the working fluid and the regenerator, thereby improving the efficiency of the regenerative process and subsequently elevating both power and thermal efficiency.

4.2.3 *Performance optimization*

The parametric analysis conducted above indicates that there exists a peak power value corresponding to the variation of the average heat transfer temperature difference. The subsequent numerical optimization aims to ascertain the maximum power of the model under diverse operating conditions.

Table 3 presents the numerical optimization results when the heat source temperature increases from 1000 to 1200 K. As shown in Table 3, the optimal heat transfer temperature difference derived from the optimization increases almost linearly with the ascending heat source temperature. However, both the magnitude and rate of increase of the optimized value δT_H are significantly larger than those of optimized value δT_L. Consequently, when maximizing the power of the Stirling engine, the optimal heat transfer temperature difference at the hot side surpasses that at the cold side. When the heat source temperature rises from 1000 to 1200 K, both the maximum output power and the corresponding thermal efficiency augment by 15.69 kW and 5.77%, respectively. A superior heat source temperature results in a higher hot side temperature level, which effectively

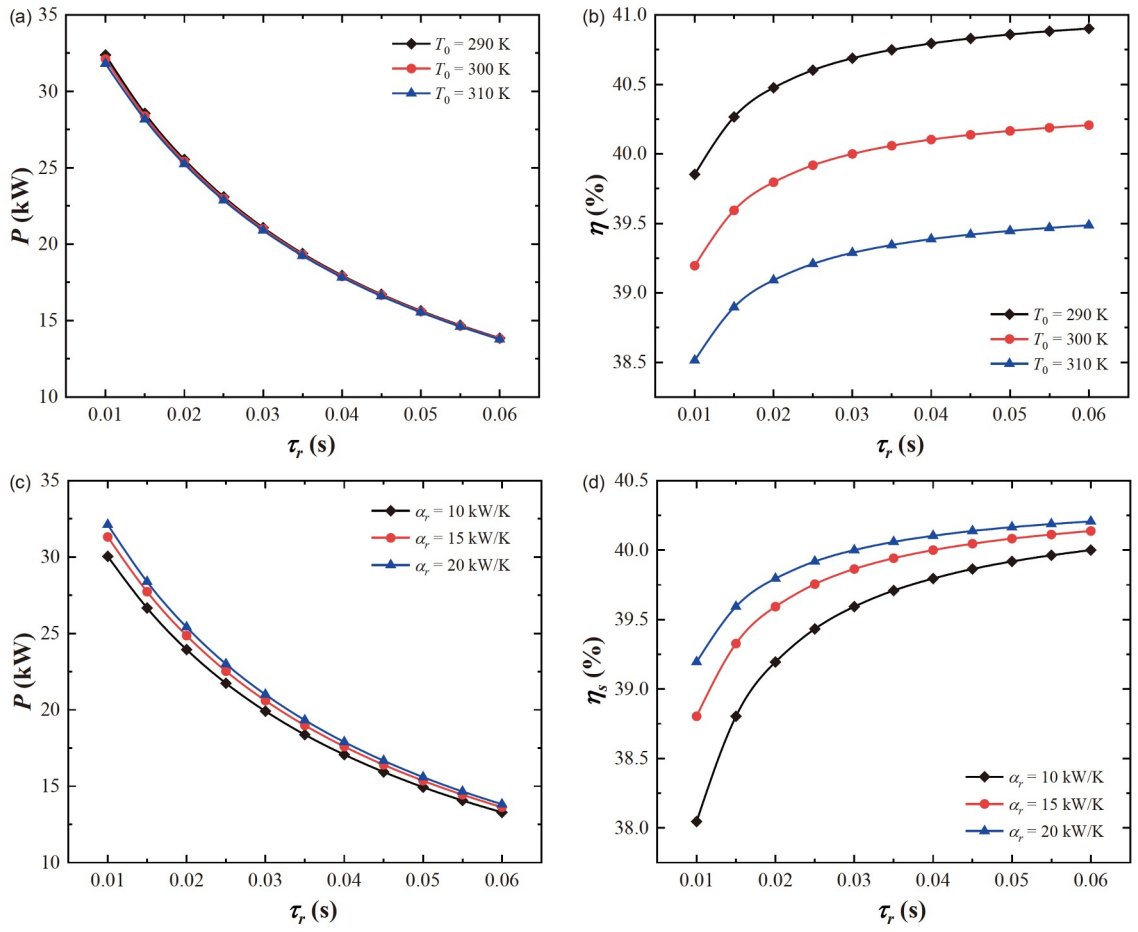

Figure 10 (Color online) Model performance as a function of regenerative cooling time. (a) Power at different ambient temperatures; (b) thermal efficiency at different ambient temperatures; (c) power at different regenerative heat transfer coefficients; (d) thermal efficiency at different regenerative heat transfer coefficients.

Table 3 Optimization results under different temperatures of heat source

T_H (K)	$\delta T_{\mathrm{H,opti}}$ (K)	$\delta T_{\mathrm{L,opti}}$ (K)	$P_{\max}$ (kW)	η (%)	Q_H (kJ)	Q_L (kJ)	τ (s)
1000	159.95	123.04	36.72	34.70	2.92	1.91	0.0276
1050	171.22	129.08	40.55	36.28	3.01	1.92	0.0270
1100	182.54	134.93	44.45	37.75	3.11	1.94	0.0264
1150	193.81	140.61	48.40	39.15	3.20	1.95	0.0259
1200	205.07	146.31	52.41	40.47	3.30	1.96	0.0255

abbreviates the heat exchange time of the cycle and augments the heat absorption of the working fluid per cycle, thereby enhancing the cycle performance.

In addition to absorbing heat from the heat source, the working fluid is also required to dissipate heat to the heat sink. Consequently, fluctuations in the heat sink temperature exert a significant influence on optimal performance. Table 4 shows the optimization results of the power at varying heat sink temperatures. When the heat sink temperature ascends from 300 to 400 K with a gradient of 25 K, both the maximum power and the corresponding thermal efficiency diminish, declining by 8.39 kW and 4.58%, respectively. As the heat sink temperature escalates, the cold side temperature level in the cycle will also rise. As observed in Table 4, with an increasing heat sink temperature, the heat absorption decreases while the heat release augments, implying a reduction in the output work of the cycle. Furthermore, the cycle time as depicted in Table 4 exhibits a slight upward trend. Therefore, both power and thermal efficiency experience a decrease due to the diminished output work and extended cycle time, as well as the narrowing temperature differential between the cold and hot sides.

As demonstrated in both Tables 5 and 6, the maximum power and the corresponding thermal efficiency ascend with

Table 4 Optimization results under different temperatures of heat sink

T_L(K)	$\delta T_{\mathrm{H,opti}}$(K)	$\delta T_{\mathrm{L,opti}}$(K)	$P_{\max}$(kW)	η(%)	Q_H(kJ)	Q_L(kJ)	τ(s)
300	159.95	123.04	36.72	34.70	2.92	1.91	0.0276
325	154.53	118.12	34.61	33.69	2.90	1.92	0.0283
350	149.09	113.86	32.50	32.57	2.89	1.95	0.0290
375	143.60	110.04	30.40	31.38	2.88	1.98	0.0297
400	138.17	106.43	28.33	30.12	2.87	2.01	0.0306

Table 5 Optimization results under different heat transfer abilities of heater

α_h(kW/K)	$\delta T_{\mathrm{H,opti}}$(K)	$\delta T_{\mathrm{L,opti}}$(K)	$P_{\max}$(kW)	η(%)	Q_H(kJ)	Q_L(kJ)	τ(s)
2	159.95	123.04	36.72	34.70	2.92	1.91	0.0276
4	124.79	133.96	44.88	35.80	3.00	1.92	0.0239
6	106.74	139.40	49.29	36.35	3.04	1.93	0.0224
8	95.04	142.77	52.19	36.70	3.06	1.94	0.0215
10	86.67	145.26	54.31	36.94	3.08	1.95	0.0210

Table 6 Optimization results under different heat transfer abilities of cooler

α_l(kW/K)	$\delta T_{\mathrm{H,opti}}$(K)	$\delta T_{\mathrm{L,opti}}$(K)	$P_{\max}$(kW)	η(%)	Q_H(kJ)	Q_L(kJ)	τ(s)
2	159.95	123.04	36.72	34.70	2.92	1.91	0.0276
4	174.49	97.57	43.36	35.48	2.93	1.89	0.0239
6	181.80	84.48	46.70	35.82	2.93	1.88	0.0225
8	186.33	76.05	48.81	36.02	2.94	1.88	0.0217
10	189.45	69.97	50.29	36.15	2.95	1.88	0.0212

the enhancement of heat transfer ability in the heater and cooler. When the heat transfer coefficients α_h and α_l increase from 2 to 10 kW/K, the maximum power and the corresponding thermal efficiency increase by approximately 17 kW and 2%, and 14 kW and 1.5%, respectively. The increased heat transfer coefficients at the hot and cold sides imply faster heat transfer rates between the working fluid and the heater, between the working fluid and cooler, respectively. Consequently, the modified Stirling cycle is completed in a significantly shorter duration, as depicted in Tables 5 and 6. Therefore, the maximum power escalates with the increased heat transfer coefficient. From Table 5, as the heat transfer coefficient α_h increases, the optimized temperature difference value δT_H rises more sharply than the decrease in the optimized temperature difference δT_L, thereby leading to an improvement in the thermal efficiency. According to Table 6, the escalation in the heat transfer coefficient α_l leads to a more substantial increase in the optimized temperature difference δT_L than the decrease in the optimized temperature difference δT_H, which is equally conducive to an increase in thermal efficiency.

4.2.4 *Multi-objective optimization*

It was observed that an increase in the heat transfer temperature difference and regenerative time results in a reduction in thermal efficiency but an escalation in power. In practical optimization problems, a single optimal solution is usually elusive due to the conflict among objectives. Multi-objective optimization can strike a balance and compromise among multiple optimization objectives to achieve an overall optimal outcome. The solution from multi-objective optimization is not a single optimal solution, but a set of Pareto solutions.

NSGA-II, a widely utilized algorithm with commendable performance for multi-objective optimization problems, improves upon NSGA in three main aspects: (1) It uses a fast non-dominated sorting algorithm to reduce the complexity of computing the non-dominated order; (2) it introduces an elite strategy to expand the sampling space and improve the accuracy of optimization results; (3) it introduces crowding and crowding comparison operators to ensure the diversity of populations. Figure 11 delineates the algorithm flow chart of NSGA-II. The key steps are as follows: Initially, fast non-dominated sorting stratifies the initial population and assigns

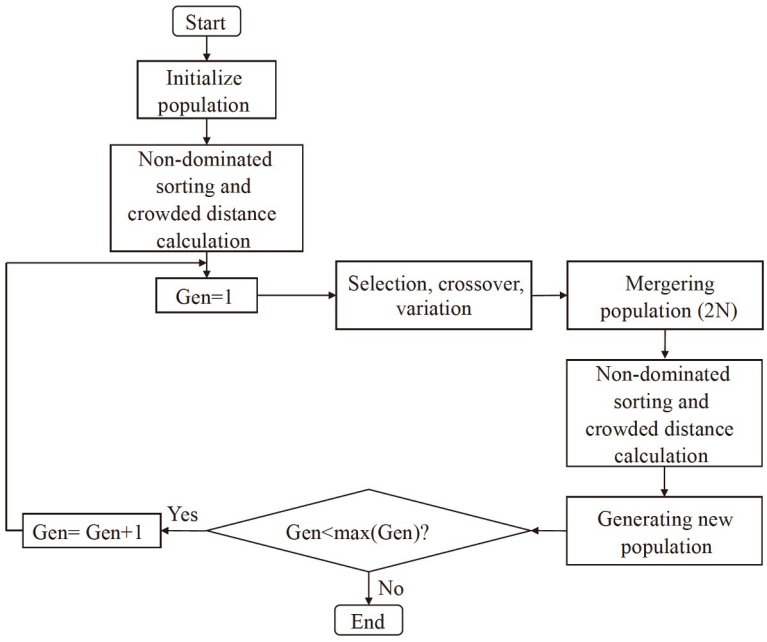

Figure 11 Flow chart of the NSGA-II algorithm.

them the same non-dominated order within each stratum. Subsequently, crowding distance selectively sorts individuals with the same non-dominated order. Finally, an elite strategy mixes parent and offspring individuals to form a new population that retains superior individuals and eliminates inferior ones.

This section presents a multi-objective optimization analysis of the irreversible modified Stirling cycle model using the NSGA-II algorithm. Table 7 provides the setting parameters of the NSGA-II algorithm.

The optimization objectives are the output power P and the thermal efficiency η, as defined by eqs. (39) and (40). The average temperature difference δT_H and δT_L, the regenerative cooling time t_{rl}, and the volume compression ratio λ, are selected as four decision variables, subject to the constraints in Table 8.

Two objectives are both maximized simultaneously in the multi-objective optimization. Figure 12 shows the Pareto front, where both ideal and non-ideal solutions are indicated. The ideal solution is located in the upper right corner of the figure, representing the maximum power and thermal efficiency. However, the trend of power and thermal efficiency is reversed: as the power increases from 7 to 43 kW, the thermal efficiency decreases from 40.5% to 36%. Furthermore, three final solutions selected by the fuzzy Bellman-Zadeh, LINMAP, and Technique for Order Preference by Similarity to an Ideal Solution (TOPSIS) decision makers are indicated in Figure 12.

Table 9 compares the decision solutions obtained from three decision methods with the corresponding results for the single objective optimization and the ideal solution. From Table 9, it can be observed that the thermal efficiency of the decision solution obtained using the fuzzy Bellman-Zadeh decision method is higher, while the power of the decision solution obtained by the LINMAP and TOPSIS decision methods is higher. To evaluate the merit of each decision solution, the deviation index d of each decision method solution from the ideal solution is presented in Table 9. The table shows that the deviation index of the solutions of fuzzy Bellman-Zadeh, LINMAP and TOPSIS decision methods are 0.1544, 0.0700 and 0.0700, respectively, and that of the single-objective optimization solutions for power and

Table 7 NSGA-II algorithm parameters

Parameter	Value
Pareto fraction	0.5
Population size	300
Generations	400
Crossover fraction	0.8

Table 8 Ranges of decision variables

Decision variable	Range	Unit
δT_H	100–240	K
δT_L	100–240	K
t_{rl}	0.001–0.008	s
λ	1.5–3	–

Table 9 Comparison of the final optimal solutions with the single objective optimization

Optimal solution	Decision making method	Decision variables				Objective		Deviation index
		δT_H(K)	δT_L(K)	t_{ri}(s)	λ	P(kW)	η(%)	d
Multi-objective optimization	FUZZY	100.53	100.16	0.0108	2.62	37.05	39.14	0.1544
	LINMAP	128.22	104.15	0.0107	2.96	40.87	37.43	0.0700
	TOPSIS	128.22	104.15	0.0107	2.96	40.87	37.43	0.0700
Max power	–	147.19	116.20	0.0107	2.95	42.26	35.87	0.0839
Max efficiency	–	100.00	100.00	0.0800	1.50	8.24	40.35	0.9161
Ideal solution	–	–	–	–	–	42.26	40.35	0.0000

thermal efficiency are 0.0839 and 0.9161, respectively. It indicates that the decision solutions of LINMAP and TOPSIS have lower deviation index. Hence, this paper uses the TOPSIS decision solution as the final desired optimal solution.

Figure 13 compares the results of multi-objective and single-objective optimizations. As shown in this figure, the TOPSIS solution trades off some power for higher thermal efficiency than the power maximization solution. It also achieves much higher power than the thermal efficiency maximization solution with a smaller efficiency loss. Therefore, the TOPSIS solution is a good compromise for increasing the power without significantly decreasing thermal efficiency.

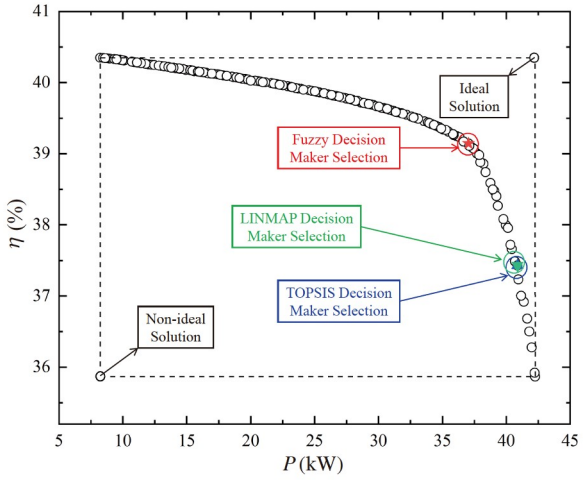

Figure 12 Pareto optimal frontier in the objective space.

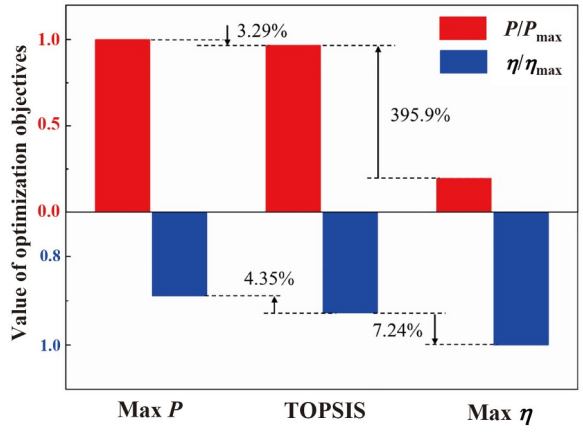

Figure 13 Performances of the different optimization methods.

5 Conclusions

This paper proposes a modified Stirling cycle model, based on the available potential function, to more accurately describe the heat transfer process of the Stirling engine and to derive an expression for the thermal efficiency. The thermal efficiency of the modified Stirling cycle is lower than that of the ideal Stirling cycle and aligns more closely with the actual Stirling engine efficiency within the same temperature range.

To further investigate the performance of the modified Stirling cycle, an irreversible modified Stirling cycle model with constant heat source, finite temperature difference heat transfer, and incomplete regenerative processes was established using the FTT method. With the modified irreversible model of Stirling cycle and corresponding algorithm, the effect of the average heat transfer temperature difference and regenerative time on the model performance was analyzed. Results indicate that the thermal efficiency of the irreversible modified Stirling cycle decreases with the increase of the average heat transfer temperature difference between the hot and cold sides, while a maximum value of the output power exists. The optimum power of the model was obtained for different heat source temperatures and heat transfer coefficients by optimizing the average heat transfer temperature difference between the hot and cold sides. The multi-objective optimization of proposed model with power and thermal efficiency as objectives showed that the LINMAP and TOPSIS decision methods result in lower deviation indexes for optimization results. Compared with single-objective optimization, multi-objective optimization balances the two objectives well. The optimal power and thermal efficiency of 40.87 kW and 44% are obtained, respectively.

This work was supported by the National Natural Science Foundation of China (Grant No. 51736004).

1 Mei S W, Chen L J. Recent advances on smart grid technology and renewable energy integration. Sci China Tech Sci, 2013, 56: 3040–3048
2 Bachmann J, Hidalgo C, Bricout S. Environmental analysis of innovative sustainable composites with potential use in aviation sector—A life cycle assessment review. Sci China Tech Sci, 2017, 60: 1301–1317
3 Niu Q, Nie C Q, Lin F, et al. Model study of relationship between local temperature and artificial heat release. Sci China Tech Sci, 2012, 55: 821–830
4 Šarauskis E, Romaneckas K, Jasinskas A, et al. Improving energy efficiency and environmental mitigation through tillage management in faba bean production. Energy, 2020, 209: 118453
5 Xu M, Lin B, Wang S. Towards energy conservation by improving energy efficiency? Evidence from China's metallurgical industry. Energy, 2021, 216: 119255
6 Singh U R, Kumar A. Review on solar Stirling engine: Development and performance. Thermal Sci Eng Prog, 2018, 8: 244–256
7 Rosato A, Sibilio S, Ciampi G. Energy, environmental and economic dynamic performance assessment of different micro-cogeneration systems in a residential application. Appl Thermal Eng, 2013, 59: 599–617
8 Damirchi H, Najafi G, Alizadehnia S, et al. Micro combined heat and power to provide heat and electrical power using biomass and Gamma-type Stirling engine. Appl Thermal Eng, 2016, 103: 1460–1469
9 Li J, Zhou Q, Mou J, et al. Neutronic design study of an integrated space nuclear reactor with Stirling engine. Ann Nucl Energy, 2020, 142: 107382
10 Dai Z, Wang C, Zhang D, et al. Design and analysis of a free-piston stirling engine for space nuclear power reactor. Nucl Eng Tech, 2021, 53: 637–646
11 Brueckner S, Miró L, Cabeza L F, et al. Methods to estimate the industrial waste heat potential of regions—A categorization and literature review. Renew Sustain Energy Rev, 2014, 38: 164–171
12 Thombare D G, Verma S K. Technological development in the Stirling cycle engines. Renew Sustain Energy Rev, 2008, 12: 1–38
13 Curzon F L, Ahlborn B. Efficiency of a Carnot engine at maximum power output. Am J Phys, 1975, 43: 22–24
14 Blank D A, Davis G W, Wu C. Power optimization of an endoreversible stirling cycle with regeneration. Energy, 1994, 19: 125–133
15 Ladas H G, Ibrahim O M. Finite-time view of the stirling engine. Energy, 1994, 19: 837–843
16 Blank D A, Wu C. Power optimization of an extra-terrestrial, solar-radiant stirling heat engine. Energy, 1995, 20: 523–530
17 Senft J R. Theoretical limits on the performance of stirling engines. Int J Energy Res, 1998, 22: 991–1000
18 Ahmadi M H, Mohammadi A H, Dehghani S. Evaluation of the maximized power of a regenerative endoreversible Stirling cycle using the thermodynamic analysis. Energy Convers Manage, 2013, 76: 561–570
19 Xu H, Chen L, Ge Y, et al. Multi-objective optimization of Stirling heat engine with various heat and mechanical losses. Energy, 2022, 256: 124699
20 Xu H, Chen L, Ge Y, et al. Four-objective optimization of an irreversible stirling heat engine with linear phenomenological heat-transfer law. Entropy, 2022, 24: 1491
21 Chen J. The effect of regenerative losses on the efficiency of a Stirling heat engine at maximum power output. Int J Ambient Energy, 1997, 18: 107–112
22 Chen J, Yan Z, Chen L, et al. Efficiency bound of a solar-driven stirling heat engine system. Int J Energy Res, 1998, 22: 805–812
23 Wu F, Chen L, Wu C, et al. Optimum performance of irreversible stirling engine with imperfect regeneration. Energy Convers Manage, 1998, 39: 727–732
24 Kaushik S C, Kumar S. Finite time thermodynamic analysis of endoreversible Stirling heat engine with regenerative losses. Energy, 2000, 25: 989–1003
25 Kaushik S C, Kumar S. Finite time thermodynamic evaluation of irreversible Ericsson and Stirling heat engines. Energy Convers Manage, 2001, 42: 295–312
26 Tyagi S K, Kaushik S C, Singhal M K. Parametric study of irreversible Stirling and Ericsson cryogenic refrigeration cycles. Energy Convers Manage, 2002, 43: 2297–2309
27 Tyagi S K, Chen J, Kaushik S C. Thermoeconomic optimization and parametric study of an irreversible Stirling heat pump cycle. Int J Thermal Sci, 2004, 43: 105–112
28 Tyagi S K, Lin G, Kaushik S C, et al. Thermoeconomic optimization of an irreversible Stirling cryogenic refrigerator cycle. Int J Refrigeration, 2004, 27: 924–931
29 Sharma A, Shukla S K, Rai Ajeet K. Finite time thermodynamic analysis and optimization of solar-dish Stirling heat engine with regenerative losses. Therm sci, 2011, 15: 995–1009
30 Tlili I. Finite time thermodynamic evaluation of endoreversible Stirling heat engine at maximum power conditions. Renew Sustain Energy Rev, 2012, 16: 2234–2241
31 Ding Z M, Chen L G, Sun F R. Performance optimization of a linear phenomenological law system Stirling engine. J Energy Institute, 2015, 88: 36–42
32 Ahmadi M H, Ahmadi M A, Mehrpooya M. Investigation of the effect of design parameters on power output and thermal efficiency of a Stirling engine by thermodynamic analysis. Int J Low-Carbon Tech, 2016, 11: 141–156
33 Dai D, Yuan F, Long R, et al. Performance analysis and multi-objective optimization of a Stirling engine based on MOPSOCD. Int J Thermal Sci, 2018, 124: 399–406
34 Dai D D, Yuan F, Long R, et al. Imperfect regeneration analysis of Stirling engine caused by temperature differences in regenerator. Energy Convers Manage, 2018, 158: 60–69
35 Zhou B, Cheng X T, Liang X G. Power output analyses and optimizations of the Stirling cycle. Sci China Tech Sci, 2013, 56: 228–236
36 Erbay L B, Yavuz H. Analysis of the stirling heat engine at maximum power conditions. Energy, 1997, 22: 645–650
37 Ozturk M M, Erbay L B. Performance analysis of the duplex Stirling refrigerator by maximum cooling load density. In: Proceedings of Energy: Production, Distribution and Conservation. Milano, 2006. 519–528
38 Babaelahi M, Sayyaadi H. A new thermal model based on polytropic numerical simulation of Stirling engines. Appl Energy, 2015, 141: 143–159
39 Hosseinzade H, Sayyaadi H, Babaelahi M. A new closed-form analytical thermal model for simulating Stirling engines based on polytropic-finite speed thermodynamics. Energy Convers Manage, 2015, 90: 395–408
40 Erbay L B, Ozturk M M, Doğan B. Overall performance of the duplex Stirling refrigerator. Energy Convers Manage, 2017, 133: 196–203
41 Dai D, Liu Z, Long R, et al. An irreversible Stirling cycle with temperature difference both in non-isothermal and isochoric processes. Energy, 2019, 186: 115875
42 Dai D, Liu Z, Yuan F, et al. Finite time thermodynamic analysis of a solar duplex Stirling refrigerator. Appl Thermal Eng, 2019, 156: 597–605
43 Lai X, Yu M, Long R, et al. Dynamic performance analysis and optimization of dish solar Stirling engine based on a modified theoretical model. Energy, 2019, 183: 573–583
44 He J, Chen J, Wu C. Ecological optimisation of an irreversible Stirling heat engine. Int J Ambient Energy, 2001, 22: 211–220
45 Yaqi L, Yaling H, Weiwei W. Optimization of solar-powered Stirling heat engine with finite-time thermodynamics. Renew Energy, 2011, 36: 421–427

46 Ahmadi M H, Hosseinzade H, Sayyaadi H, et al. Application of the multi-objective optimization method for designing a powered Stirling heat engine: Design with maximized power, thermal efficiency and minimized pressure loss. Renew Energy, 2013, 60: 313–322

47 Ahmadi M H, Mohammadi A H, Dehghani S, et al. Multi-objective thermodynamic-based optimization of output power of solar dish-Stirling engine by implementing an evolutionary algorithm. Energy Convers Manage, 2013, 75: 438–445

48 Ahmadi M H, Sayyaadi H, Dehghani S, et al. Designing a solar powered Stirling heat engine based on multiple criteria: Maximized thermal efficiency and power. Energy Convers Manage, 2013, 75: 282–291

49 Ahmadi M H, Sayyaadi H, Mohammadi A H, et al. Thermo-economic multi-objective optimization of solar dish-Stirling engine by implementing evolutionary algorithm. Energy Convers Manage, 2013, 73: 370–380

50 Duan C, Wang X, Shu S, et al. Thermodynamic design of Stirling engine using multi-objective particle swarm optimization algorithm. Energy Convers Manage, 2014, 84: 88–96

51 Toghyani S, Kasaeian A, Ahmadi M H. Multi-objective optimization of Stirling engine using non-ideal adiabatic method. Energy Convers Manage, 2014, 80: 54–62

52 Patel V, Savsani V. Multi-objective optimization of a Stirling heat engine using TS-TLBO (tutorial training and self learning inspired teaching-learning based optimization) algorithm. Energy, 2016, 95: 528–541

53 Zare S, Tavakolpour-saleh A R, Aghahosseini A, et al. Design and optimization of Stirling engines using soft computing methods: A review. Appl Energy, 2021, 283: 116258

54 Eser S, Yuce B E. A metaheuristic approach for multi-objective optimization of the Stirling cycle with internal irreversibilities and regenerative losses using artificial bee colony algorithm. Energy Convers Manage, 2023, 292: 117372

55 Yu M, Shi C, Liu Z, et al. Design and multi-objective optimization of a new annular constructal bifurcation Stirling regenerator using response surface methodology. Int J Heat Mass Transfer, 2022, 195: 123129

56 Chen L, Shi S, Ge Y, et al. Ecological function performance analysis and multi-objective optimization for an endoreversible four-reservoir chemical pump. Energy, 2023, 282: 128717

57 Bejan A. Entropy generation minimization: The new thermodynamics of finite-size devices and finite-time processes. J Appl Phys, 1996, 79: 1191–1218

58 Klein S, Nellis G. Thermodynamics. Cambridge: Cambridge University Press, 2011

59 Liu W, Liu P, Wang J B, et al. Exergy destruction minimization: A principle to convective heat transfer enhancement. Int J Heat Mass Transfer, 2018, 122: 11–21

60 Martini W R. Stirling Engine Design Manual. Second edition. Contractor Report. Richland: Martini Engineering, 1983